Journal of Materials Science: Materials in Electronics (2019) 30:6984–6992
https://doi.org/10.1007/s10854-019-01016-6

Influence of the spark-plasma texturing conditions on the intragranular features of Bi-2223 ceramic samples

L. Pérez-Acosta[1] · E. Govea-Alcaide[2,3] · F. Rosales-Saiz[3] · J. G. Noudem[4] · I. F. Machado[5] · R. F. Jardim[6]

Received: 1 October 2018 / Accepted: 25 February 2019 / Published online: 8 March 2019

Abstract
The influence of the spark-plasma texturing (SPT) conditions on the intragranular superconducting properties of $Bi_{1.65}Pb_{0.35}Sr_2Ca_2Cu_3O_{10+\delta}$ (Bi-2223) samples has been investigated. Also, the SPT samples were subjected to a post-annealing heat treatments (PAHT) in different times. Intragranular superconducting features, extracted from magnetoresistance measurements, $\rho(T, H)$, in applied magnetic fields up to 9 T, were studied by analyzing the temperature dependence of the in-plane upper critical field, $H_{c2}^{ab}(T)$, and the magnetic field dependence of the pinning energy at zero temperature, $U(0, H)$. The results indicated that, before and after the PAHT, values of the $H_{c2}^{ab}(0)$, obtained by using the Werthamer–Helfand–Hohenberg formula, increased ~ 21%, i.e., from 115.8 to 140.2 T. We have also found that the effective intragranular pinning energy at zero applied magnetic field, $U_0 = U(0, 0)$, also increased over approximately three times, from 0.28 to 0.98 eV. These results strong strongly indicate that the SPT process is responsible for inducing deoxygenation at the intragranular level of ceramic samples, a feature presumably occurring near of the end of planar defects.

1 Introduction

As far as the densification of powders is concerned, the conventional spark-plasma sintering (SPS) is a very useful method and largely employed in the last decades [1, 2]. In the SPS process, sintering is achieved in very short time intervals by the simultaneous action of the electric current and applied compacting pressure. An alternative method, namely spark-plasma texturing (SPT), together with a better densification is also responsible for the improvement of the degree of texture in different classes of materials [3]. In $(Bi,Pb)_2Sr_2Ca_2Cu_3O_{10+y}$ (Bi-2223) superconductor, the application of the SPT technique results in samples with relative density close to 96% of the theoretical value and very high texture degree, even when low uniaxial compacting pressure of 50 MPa is used [4].

Similarly to the SPS technique, consolidation of powders through the SPT method is conducted under vacuum of ~ 10 to 30 Pa. This unavoidable condition, along with the application of elevated electrical current during the sintering, has a definite impact on the microstructure of the resulting materials, e.g., at the grain boundaries [4]. For instance, Bi-2223 samples consolidated by the SPT method are composed of grains with core–shell morphology. In such a morphology, the core of the grains is comprised of stoichiometric Bi-2223 and the shell is formed essentially by Bi-2223, but with oxygen deficiency. Due to the close relationship between the superconducting properties and the oxygen content, the Bi-2223 samples consolidated by the SPT method must be subjected to a post-annealing heat treatment (PAHT) [4, 5]. However, previous works were focused on the effect of the sintering conditions on the intergranular features of the samples. However, an experimental study of the impact of the SPT consolidation on the intragranular superconducting properties of ceramic samples is lacking.

✉ E. Govea-Alcaide
egoveaalcaide@gmail.com

[1] Departamento de Física, Facultad de Informática y Ciencias Exactas, Universidad de Camagüey, Camagüey, Cuba

[2] Departamento de Física, Universidade Federal do Amazonas, Manaus, Brazil

[3] Departamento de Matemática-Física, Facultad de Ciencias Informáticas, Naturales y Exactas, Universidad de Granma, Bayamo, Cuba

[4] Normandie Univ, ENSICAEN, UNICAEN, CNRS, CRISMAT, 14000 Caen, France

[5] Departamento de Engenharia Mecatrônica e Sistemas Mecânicos, Escola Politécnica, Universidade de São Paulo, São Paulo, SP, Brazil

[6] Departamento dos Física de Materiais e Mecânica, Instituto de Física, Universidade de São Paulo, São Paulo, Brazil

Within this context, we have performed a systematic study of the resistive transition in $Bi_{1.65}Pb_{0.35}Sr_2Ca_2Cu_3O_{10+\delta}$ ceramic samples obtained through the SPT method. The influence of the consolidation parameters on the phase composition and microstructure of the samples was inferred from X-ray diffraction (XRD) analysis performed in powder and pellet samples along with finite element simulation methods. The main contribution of this work is to discuss the influence of consolidation conditions on the intragranular superconducting properties of Bi-2223 compounds and the role played by the post-annealing heat treatment. Also, finite element simulations of the SPT process were performed to investigate the relationship between the consolidation conditions and the phase composition and microstructure of the obtained samples.

2 Materials and methods

Pre-reacted powders of $Bi_{1.65}Pb_{0.35}Sr_2Ca_2Cu_3O_{10+\delta}$ (Bi-2223) have been synthesized by using the conventional solid state reaction method, as described in details in the reference [6]. For the SPT consolidation, the pre-reacted Bi-2223 powders were first shaped into pellets with a mean diameter of $\sim$ 13 mm by applying a uniaxial compacting pressure of 30 MPa. The shaped pellets were pre-sintered in a furnace at 700 °C for 120 min in air. After this step, the pellets can be easily accommodated at the center of a graphite die of a larger diameter of $\sim$ 20 mm. Under this condition, a difference of 3.5 mm between the radius of the pellet and the inner radius of the graphite die is settled [3]. The final processing of the pellets was carried out by using the SPSS apparatus FCT System GmbH, HP D25, Rauenstein, Germany. The consolidation was performed under vacuum (from 10 to $\sim$ 30 Pa) and the maximum uniaxial compacting pressure used was 50 MPa. Other sintering conditions were: consolidation temperature, $T_D = 750$ °C, heating rate, $HR = 100$ °C/min, and dwell time, $t_D = 15$ min. Samples processed by the procedure described above will be referred to as ST0. After the SPT consolidation, small pieces of the samples were subjected to an additional, oxygenation post-annealing heat treatment (PAHT) performed in a Lindberg/Blue tubular furnace at 750 °C in air by using a heating rate of $HR = 5$ °C/min, and for two time intervals: 5 and 30 min. These samples will be hereafter referred to as ST5 and ST30, respectively.

The phase identification of the samples was evaluated from X-ray diffraction patterns obtained in a Bruker-AXS D8 Advance diffractometer. These measurements were performed at room temperature using CuKα radiation in the $3° \leq 2\theta \leq 80°$ range with a $0.05°(2\theta)$ step size, and 5 s counting time. X-ray measurements were performed in powder and pellets samples. In the later case, the patterns were measured in two surfaces of the samples. The first, where the piston used in the compacting process has direct mechanical contact with the powder, referred to as face-S and the other one, which is perpendicular to the former, referred here to as face-L. We mention that S and L are perpendicular and parallel to the compacting direction, respectively. The volume density, ρ_v, of all pellets was determined by using the Archimedes method.

The temperature and magnetic field dependence of the electrical resistivity $\rho(T, H)$ were measured by using the four-probe method in a Quantum Design Dynacool Physical Property Measurement System (PPMS), operating in the T and H ranges of 1.8–300 K and 0–9 T, respectively. The typical dimensions of the samples were $d = 0.5$ mm (thickness), $w = 2$ mm (width), and $l = 10$ mm (length). In these measurements Au electrical leads were attached to Ag film contact pads on samples. After cooling the sample under zero applied magnetic field, an excitation current, I, of 1 mA ($J = 10^{-2}$ A/cm^2) was injected along the major length of samples. The magnetic field, H, was applied parallel to the uniaxial compacting pressure direction and perpendicular to I.

3 Finite element method simulations

The SPSS apparatus used to consolidate our ceramic samples does not allow the measurement of the actual temperature within the sample region. For this reason, the finite element simulation has been used to gain extra information regarding the actual temperature experienced by the samples during the spark-plasma process [7–9]. The schematic drawing of the consolidation system and the boundary conditions limited by the apparatus are displayed in Fig. 1a, b. The arrangement consist of two Inconel electrodes, six graphite spacers, the die with two plungers surrounding the sample, that is located in the center of the stack. In this case, Fig. 1c displays both the SPS and SPT setups, respectively. Taking into account the axisymmetrical configuration, only two dimensions are of the interest, the system is studied in cylindrical coordinates, and the problem is rather simplified. For every domain displayed in Fig. 1a, the spark-plasma process is governed by a system of electro–thermal–mechanical coupled partial differential equations related to the heat transfer process, the charge conservation, and constitutive equations for a linear elastic problem given by [7, 8]

$$\nabla \times J = 0 \tag{1}$$

$$\rho c_p(T)\frac{\partial T}{\partial t} - \nabla \times (k\nabla T) = \dot{q}_J \tag{2}$$

$$\nabla \times \sigma + F = 0 \tag{3}$$

where T is the temperature; ρ is the density, here assumed to be constant and corresponding to the last stage of sintering; $\dot{q}_J = J \times E$ is the heat loss by Joule effect; $J = E/\rho_e(T)$ is the electric current density; $\rho_e(T)$ is the temperature dependence

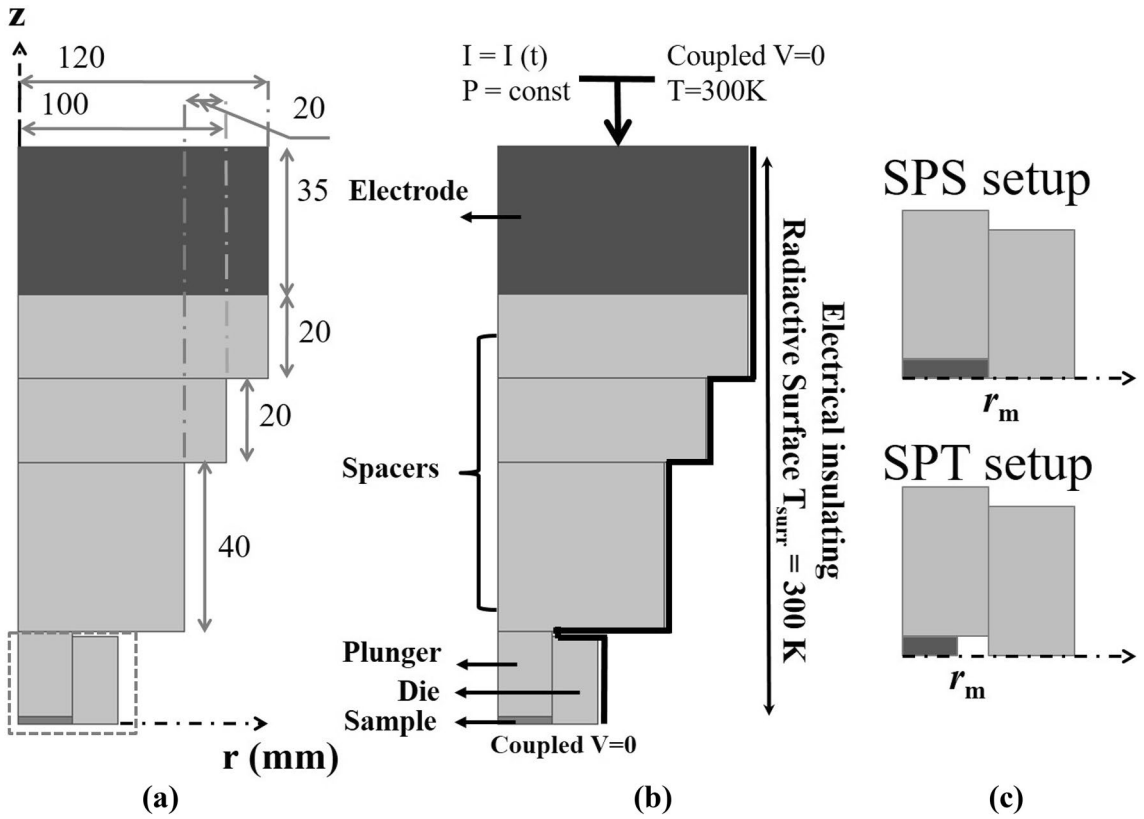

Fig. 1 **a** Schematic drawing of the consolidation system; **b** boundary conditions; **c** SPT and SPS plunger/die setups

of the electrical resistivity; $c_p(T)$ and $k(T)$ are the temperature dependence of the heat capacity and thermal conductivity, respectively; σ is the stress tensor, and F, the body force per unit volume. Values for all parameters are assigned for each material or domain in the actual design, i.e., the Inconel 600, the high-density graphite, and the Bi-2223 ceramic sample. Table 1 displays the parameters used in the FEM simulations.

The initial and boundary conditions used for solving eqs. (1), (2), and (3) are displayed in Fig. 1b. The initial temperature was set to be 300 K and the heat losses by conduction and/or convection through the gas were neglected because the process occurs in vacuum. All the free surfaces exposed to the vacuum chamber have heat losses by radiation and are given by $\dot{q}_{rad} = \sigma_s \varepsilon (T_d^4 - T_0^4)$, where T_d is the temperature of the free surfaces, σ_s the Stefan-Boltzmann's constant, $\varepsilon = 0.3$ (0.69) is the graphite (Inconel 600) emissivity, and

Table 1 Parameters of Bi-2223 samples, graphite, and Inconel 600 used in the FEM simulations: ρ is its density, $\rho_e(T)$ is the electrical resistivity as a function of temperature, $c_p(T)$ is the heat capacity as a function of temperature, and $k(T)$ is the thermal conductivity

Property	Bi-2223	High-density graphite	Inconel 600	Units
ρ	5700*	1900	8175	kg/m^3
$\rho_e(T)$	$0.8 \times 10^{-6} + 0.8 \times 10^{-8} T$	$2.4 \times 10^{-5} - 2.6 \times 10^{-8} T + 2.2 \times 10^{-11} T^2$	$1.03 \times 10^{-6} - 1.85 \times 10^{-10} T + 6.2 \times 10^{-13} T^2$	Ω m
$c_p(T)$	$131.6 + 0.77T$	$-151 + 2.3T - 7.1 \times 10^{-4} T^2$	$395.28 + 0.1576T + 7.1 \times 10^{-5} T^2$	J/(kg K)
$k(T)$	$0.27 + 1.95 \times 10^{-3} T$	$84 - 0.063 \times T + 2.9 \times 10^{-5} \times T^2$	$8.955 + 0.016T$	W/(m K)
Young's modulus	51.15×10^9	1.03×10^{11}	$-2.841 \times 10^4 T^2 - 2.866 \times 10^7 T + 2.666 \times 10^{11}$	Pa
Poisson's ratio	0.166	0.32	0.315	Pa
Thermal expansion	18×10^{-6}	8×10^{-6}	1.5×10^{-5}	Pa

$T_0 = 300$ K is the temperature of the wall chamber. The temperature of both the upper and lower Inconel electrodes was 300 K and the electrical and thermal resistances were disregarded [7]. Finally, the electro–thermal–mechanical eqs. (1), (2), and (3) were solved by using the COMSOL Multiphysics™ package. Also, a proportional–integral–derivative (PID) control has been programmed into the COMSOL code. In this particular case, the current profile $I(t)$ is given by

$$I(t) = k_P e(t) + k_I \int_0^t e(t)dt + k_D(de(t)/dt), \quad (4)$$

where $e(t)$ is the difference between the desired temperature and the actual temperature of the control point. It is important to point out that $I(t)$ is applied as a function of the measured temperature as a close-loop control system. Values of k_P, k_I, and k_D are then obtained by adjusting the PID control to the experimental temperature profile [9].

4 Results and discussion

Figure 2 displays the X-ray diffraction patterns taken on the pre-reacted powder, and bulk samples ST0, ST5, and ST30. The X-ray data of bulk samples were taken along the surface L. By comparing bulk and powder patterns, it is clear that all samples have similar chemical composition and their indexed reflections are related to the high-T_c Bi-2223 phase [4]. The unit-cell parameters were calculated regarding an orthorhombic unit cell and the obtained values $a = 5.409$ Å, $b = 5.411$ Å, and $c = 37.153$ Å are in line with those reported elsewhere for the same compound [6]. We have also found that the post-annealed samples ST5 and ST30 exhibit an additional peak located at $2\Theta = 33.18°$. Such a Bragg reflection is related to the most intense peak belonging to an infinite layer compound $Ca_{1-x}Sr_xCuO_2$, as discussed elsewhere [10]. We have also found that the height of this extra peak remains almost unaltered as the PAHT time increased from 5 to 30 min, suggesting that changes in the time interval of the PAHT has no influence on the phase content of the samples.

Additionally, from patterns displayed in Fig. 2 it was possible to estimate the ratio between the height of peaks (00*l*) and (*hkl*), yielding a value of 0.35 for the pre-reacted powder and ~ 0.29 for all SPT samples. By assuming that these values can be considered as a roughly measure of the degree of texture of the samples, the obtained result seems to be paradoxical because the degree of texture of powder samples is greater than the pellet ones. However, we first argue that the X-ray data of ST0, ST5, and ST30 samples were taken along the surface L, which is parallel to the compacting pressure direction. As the application of the SPT technique aims to produce high textured samples [3, 4], the degree of texture along this surface is expected to be very low. In order to verify such a statement, Fig. 3a, b display the X-ray diffraction patterns taken along surfaces L and S, respectively. The difference of the degree of texture between both surfaces is verified visually by inspecting the height of the peaks (113) – (00l0), and (200) – (0014), respectively (see dashed boxes). In addition, the most intense reflection

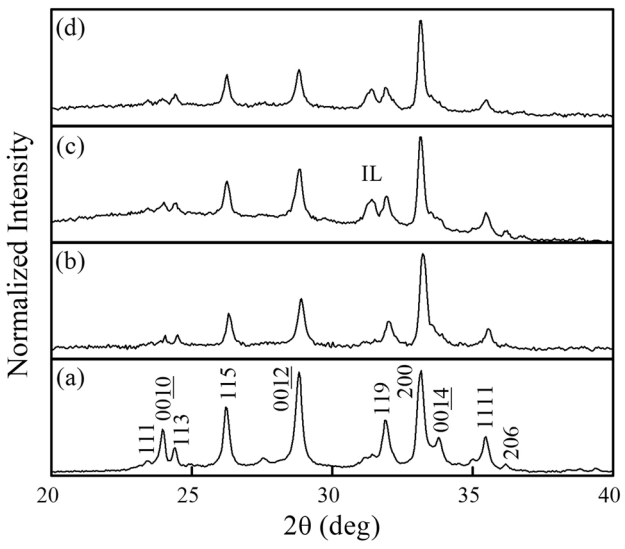

Fig. 2 X-ray diffraction patterns taken in the pre-reacted powders (a) and in pellets of the SPT samples ST0 (b), ST5 (c), and ST30 (d). In the pellet samples, measurements were performed along the surface L, and in panel (c), IL refers to an infinite layer compound with the general formula $Ca_{1-x}Sr_xCuO_2$. Also, Bragg reflections belonging to the Bi-2223 phase are marked by Miller indexes in (a)

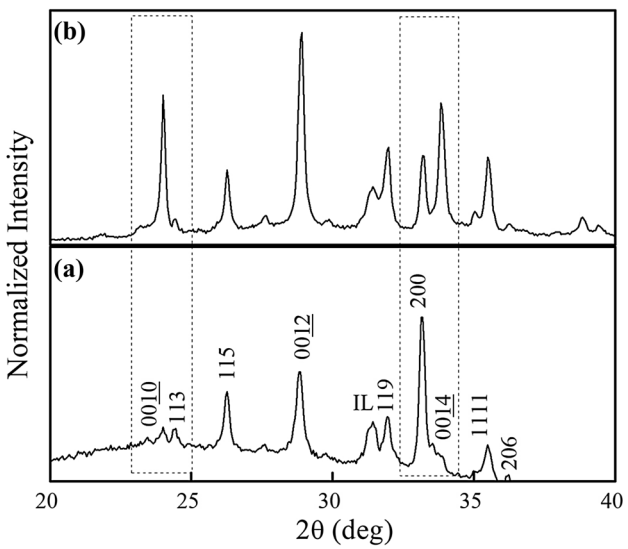

Fig. 3 X-ray diffraction patterns taken in the pellet sample ST5. The measurement were performed along the surfaces L (a) and S (b). Bragg peaks of the Bi-2223 phase are identified by their Miller indexes in (a). Selected regions of the diagrams, marked as dashed boxes, are discussed in the text

of the diagrams taken along surface L is (200), in contrast to the one from the surface S, (0012). A quantitative evaluation of the degree of texture along the surface S yields 0.59, a value twice higher than that obtained along the surface L.

Computational simulations were performed to have a clear understanding about the influence of the SPT process on the phase composition and the microstructure of the samples. For comparison reasons, simulations were also performed considering the SPS pluger/die setup (see Fig. 1c). Figure 4a, b show the results of the computational simulation of the temperature, $T(r_m, z)$, and the normalized radial stress distribution, $\sigma(r_{mm}, z)/\sigma(r_m, 0)$, respectively, for the SPT pluger/die setup (see Fig. 1c). Here r_m is the radius of the sample. Both distributions were taken along the vertical direction, z, and at $t = 8$ min, i.e., at a given moment during the sintering time interval.

As can be seen in Fig. 4a, the difference in temperature between both configurations is close to 0.1 °C and the qualitative behavior of both curves is very similar. Along the z-direction, the estimated difference in temperatures between the center of the sample ($r = 0$) and its outer surface ($r = r_m$) is pretty small, less than 1 °C, and may be disregarded. Here, we must recall that the optimum sintering temperature for the Bi-2223 phase is ~ 845 °C and the predefined temperature at the thermocouple position (consolidation temperature) was 750 °C. Thus, our findings indicate that under our experimental consolidation conditions the temperature of the samples is significantly below ~ 845 °C. This corroborates our finding that the SPT conditions applied here do not affect the phase composition of samples, a result in agreement with X-ray diffraction analysis.

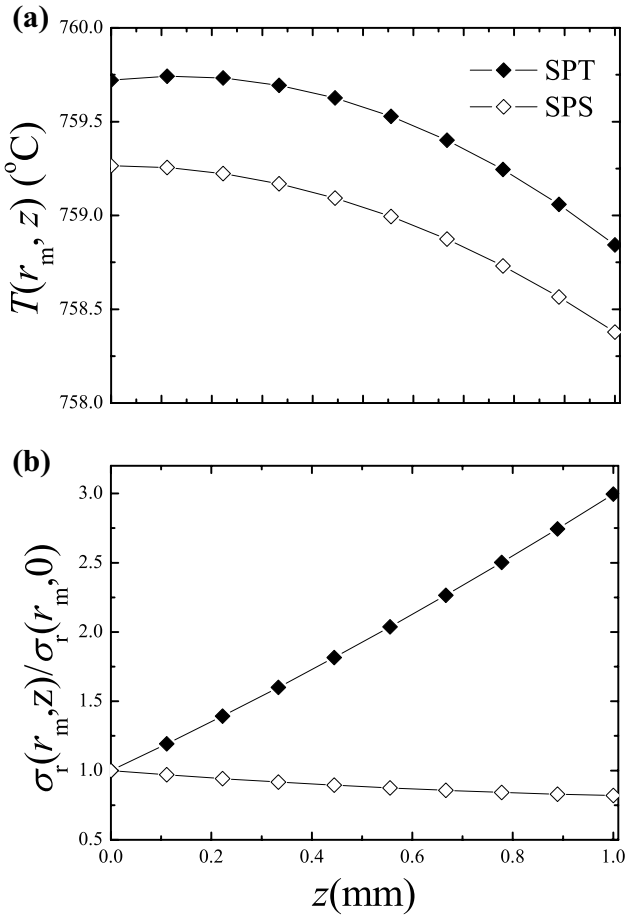

Fig. 4 Temperature (**a**) and radial stress (**b**) distributions along the outer wall of SPT and SPS samples. All curves were obtained for a simulation time of $t = 500$ s

Figure 4b displays the normalized radial stress distribution along the z-direction for $r = r_m$. As expected, the major difference between the SPS and the SPT techniques is related to the influence of the stress distribution on the microstructure of the samples. In this case, the results indicate that the ratio $\sigma(r_{m\,m}, z)/\sigma(r_m, 0)$ for the SPS configuration is almost pressure independent and the higher value of the stress is attained for $z = 0$. On the other hand, in the SPT plunger/die setup, the ratio $\sigma(r_{m\,m}, z)/\sigma(r_m, 0)$ exhibits an appreciable pressure dependent behavior. Under this configuration, the maximum stress value is seen in a point at the edge of the sample in contact with the plunger for $r = r_m$. These findings indicate that the SPT configuration is responsible for a pronounced mechanical impact on the microstructure than the other one. In fact, such a configuration allows the lateral wall of the sample to move freely along the r_m direction, resulting in a better alignment of the anisotropic grains of the Bi-2223 material, as reported elsewhere [3, 4].

On the other hand, Fig. 5a–c display the $\rho(T, H)$ curves of samples ST0, ST5, and ST30, respectively, under the influence of applied magnetic fields ranging from 0 to 9 T. We have found that the progressive increase of the magnetic field results in appreciable changes in the shape of the resistive transition to the superconducting state, a feature observed in all samples studied. As the magnetic field increases in strength, the transition becomes broader. We have also found that all curves exhibit a transition to the superconducting state below the so-called onset critical temperature $T_{on} \sim 120$ K. Besides, the temperature in which the zero resistance state is observed, the offset temperature, T_{off}, decreases abruptly with increasing H. For the same applied magnetic field window ($H = 0 - 9$ T), it was found that T_{off} decreases in the range 88.5–35.5 K in ST0, 96.1–38.6 K in ST5, and 92.3–35.7 K, in ST30. It is important to point out that the observed values of T_{off} at $H = 0$ T are slightly lower when compared with previous results of ~ 102 K in Bi-2223 materials [6]. This is a consequence of the remanent magnetic field of the superconducting magnet.

We have already mentioned that the SPT consolidation takes place under vacuum, resulting in samples composed of grains with a core–shell morphology, i.e., grains with a core of stoichiometric Bi-2223 phase and an

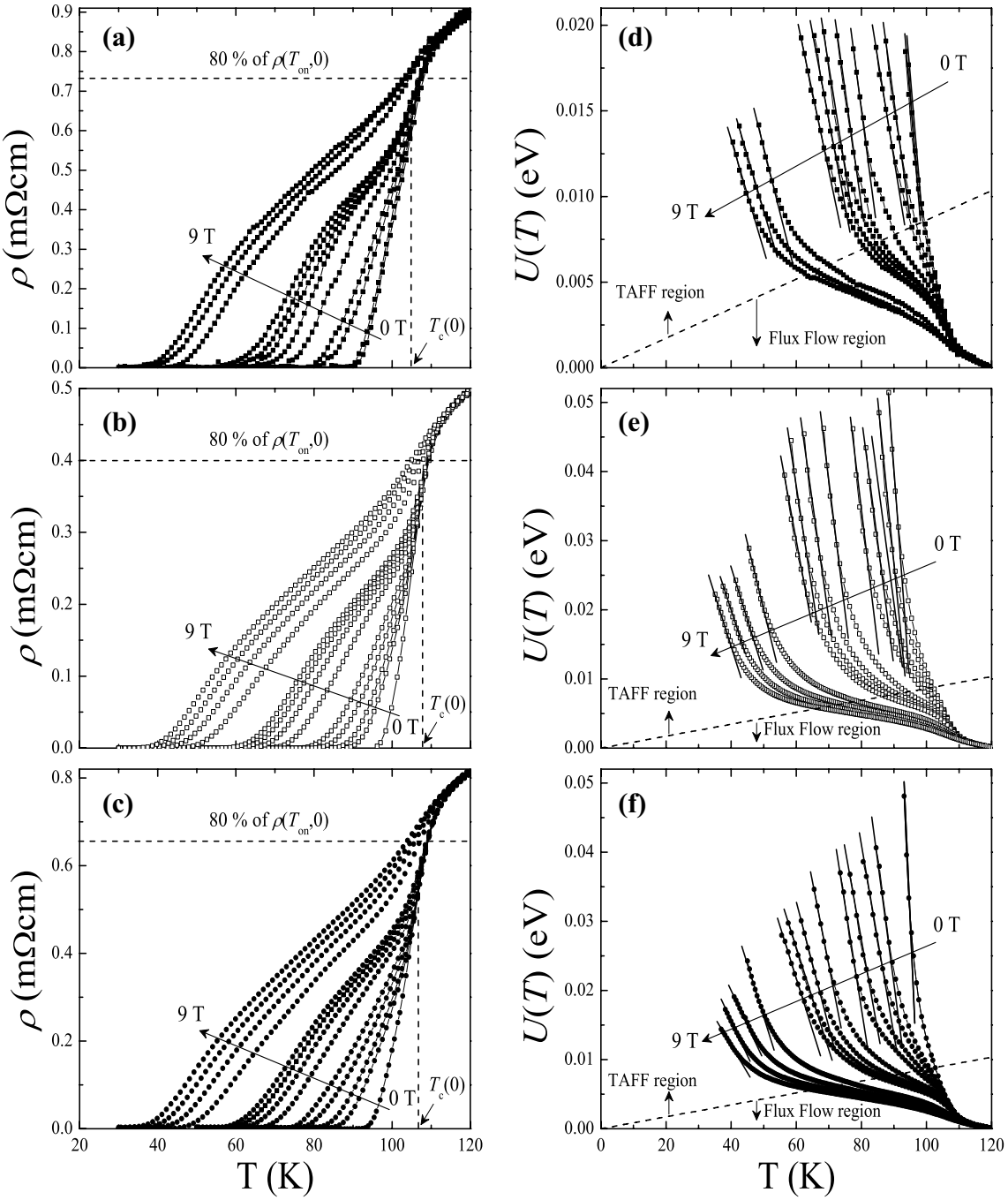

Fig. 5 Electrical resistive transition in applied magnetic fields up to 9 T of samples ST0 (**a**), ST5 (**b**), and ST30 (**c**). Values of the upper critical field H_{c2} were obtained from the 80% drop in $\rho(T, H)$ curves across the superconducting transition. The temperature dependence of the activation energies for samples ST0, ST5, and ST30 are displayed in **d**–**f**), respectively. Dashed lines correspond to $U(T) = k_B T$ and separate the flux-flow conductivity from the thermally activated flux-flow (TAFF) regime

oxygen-deficient shell [4]. Assuming this kind of morphology sets up in our samples, it is possible to understand the difference in T_{off} between samples ST0, ST5, and ST30 (see Table 2). We first mention that values of $T_{off}(0)$ are strongly influenced by the intergranular features in granular superconductors . Thus, in the ST0 sample, even with a relative density as high as 96% and with a high degree of texture [4], the core–shell morphology is sufficient in promoting a weak-link behavior at the intergranular level of the material. On the other hand, after the PAHT the intergranular properties of the samples are partially restored and $T_{off}(0)$ is observed to increase from 88.5 to 96.1 K,

Table 2 Some relevant parameters of the SPT samples: $T_{off}(0)$ and $T_c(0)$ are the offset critical temperature and the critical temperature at zero applied magnetic field, respectively, $-dH_{c2}(0)/dT$ is the slope of $H_{c2}(T)$ curve, $H_{c2}^{ab}(0)$ is the orbital upper critical field at $T = 0$ K, and $U_0(0)$ is the intragranular pinning energy

Sample	$T_{off}(0)$ (K)	$T_c(0)$ (K)	$-dH_{c2}(0)/dT$ (T/K)	$H_{c2}^{ab}(0)$ (K)	U_0 (eV)
ST0	88.5	104.3	1.61	115.8	0.28
ST5	96.1	108.1	1.88	140.2	0.98
ST30	92.3	106.2	1.65	120.9	0.93

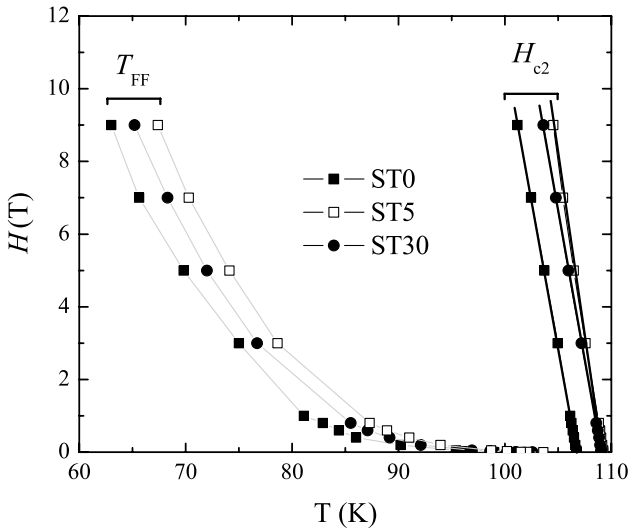

Fig. 6 Vortex phase diagram of Bi-2223 samples ST0, ST5, and ST30 (see details in the text)

as seen in sample ST5. It is also interesting to point out that an increase in the post-annealing time interval from 5 to 30 min results in a decrease in $T_{off}(0)$ of ~ 4 K . It seems that increasing the post-annealing time results in a deterioration the superconducting properties of the grain boundaries.

From the $\rho(T,H)$ data, we were able to built an H_{c2}-T phase diagram of the studied samples and the results are displayed in Fig. 6. Pairs of (H,T) were extracted from the $\rho(T,H)$ curves by using the $\rho(T,H)/\rho(T_{on}) = 0.5$ criterion [11–14]. However, when polycrystalline samples are considered, the application of such a criterion may introduce artifacts stemming from the intergranular contribution. This occurs when the superconducting critical temperature at zero magnetic field, $T_c(0) = (T_{on} + T_{off}(0))/2$ is greater than the temperature where the condition $\rho(T,0)/\rho(T_{on}) = 0.5$ is valid. Taken into account values of $T_c(0)$ listed in Table 2 and to assure that only the intragranular contribution must be considered, we adopted the $\rho(T,H)/\rho(T_{on}) = 0.8$ criterion for all samples (see Fig. 5a–c).

The results displayed in Fig. 6 reveal a linear relationship between H_{c2} and T near $T_c(0)$ in all samples. The orbital upper critical field at $T = 0$ can be estimated by using the Werthamer–Helfand–Hohenberg (WHH) formula $H_{c2}(0) = 0.69T_c(0)(dH_{c2}(T)/dT)$, where $-(dH_{c2}(T)/dT)$ is the linear slope of the $H_{c2}(T)$ dependence. Also, considering the measurements conditions (H parallel to the compacting pressure) and the high degree of texture of the samples, it is reasonable to assume that the estimated values of $H_{c2}(0)$ mostly reflect the upper critical field parallel to the *ab*-plane, $H_{c2}^{ab}(0)$. Thus, the results for $H_{c2}^{ab}(0)$ yielded 115.8, 140.2, and 120.9 T for samples ST0, ST5, and ST30, respectively (see Table 2). The above values are in the range 40–350 T and in line with those previously reported for Bi-2223 ceramic samples [15–17].

It is important to point out that the extrapolated value $H_{c2}^{ab}(0)$ increases $\sim 21\%$ between samples ST0 and ST5. Previous results indicate that these samples have similar phase composition and degree of texture. Hence, such an increase in $H_{c2}^{ab}(0)$ is only related to the influence of the post-annealing heat treatment, further suggesting that the deoxygenation caused by the SPT sintering can also affect the intragranular superconducting properties of the samples. To our knowledge, this is a new finding, which has not been reported in previous studies regarding superconducting cuprates obtained by using spark-plasma sintering techniques [4–6].

Another way to evaluate the influence of SPT conditions on the intragranular features of the ceramic samples is by inspecting its pinning capabilities. Figure 5d–f display the temperature and applied magnetic field dependence of the pinning energy, $U(T,H)$, for samples ST0, ST5, and ST30, respectively. These curves were constructed by recalculating the experimental electrical resistivity data as $U(T,H) = k_B T \ln(\rho(T_{on})/\rho(T,H))$ [11]. The dashed lines in the Fig. 5d–f indicated boundary lines that separates the flux-flow (FF) region from the thermally activated flux-flow regime (TAFF), i.e., the temperature T_{ff} where $U(T,H) = k_B T$ [11]. Figure 6 shows T_{ff} vs. H boundary lines for samples ST0, ST5, and ST30. As observed, all curves exhibit similar downward curvature and, in all range of the applied magnetic field, values of T_{ff} in sample ST5 when compared with those from samples ST0 and ST30, respectively. Provided that the TAFF region has been identified, the $U(T, H)$ curves were linearly extrapolated to $T = 0$ K and values of the applied magnetic field dependence of the effective pinning energy, $U(0, H)$, were obtained.

Figure 7 displays the magnetic field dependence of $U(0, H)$ for samples ST0, ST5, and ST30. Also, in the inset of Fig. 7 are shown fittings of the experimental data to the equation $U(0, H) \propto H^{-\alpha}$, where α is an exponent. The results yield $\alpha = 0.15$, 0.5, and 0.28 for samples ST0, ST5, and ST30 respectively. These values are close to those expected for highly anisotropic materials such as

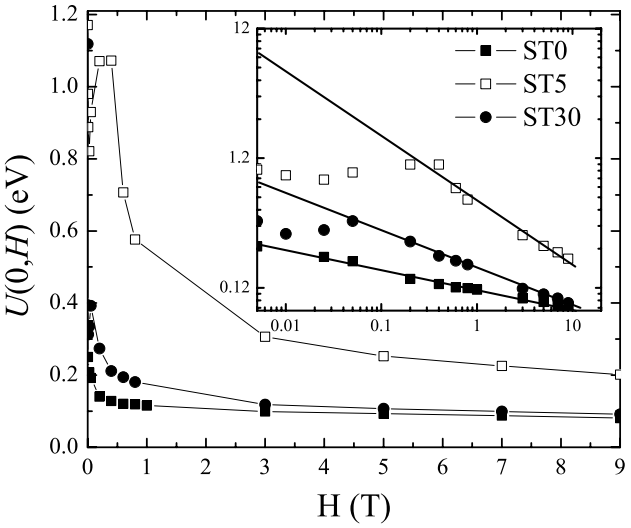

Fig. 7 Effective pinning energy as a function of applied magnetic field, $U(0, H)$, for samples ST0, ST5, and ST30. The inset shows the fit of the experimental data to $U(0, H) \propto H^{-\alpha}$. In this case, the fitting curves are displayed in solid lines

the BSCCO compounds [11, 18] and indicate that the vortex dimensionality of the studied samples is 2D, at least, for $H \geq 1$T. Additionally, values of the effective pinning energy at zero applied magnetic field, $U_0 = U_0(0, 0)$, for samples ST0, ST5, and ST30 are listed in the Table 2. In particular, a 3.5-fold increase in U_0 is observed between samples ST0 and ST5. This result suggest that the SPT process is responsible for a pronounced suppression of the intragranular pinning capabilities of the samples. We speculate that, as the SPT process occurs under vacuum, the deoxygenation occurs preferentially within the grains, and predominantly at the edge of planar defects, e.g, stacking faults [19]. Such imperfections act, similarly to grain boundaries, as a current-blocking defects which locally increases the Joule self-heating effect. It seems that the combination of effects arising from high electric current during the sintering, the increase of the local temperature at the edge of planar defects, and vacuum, result in the oxygen electromigration. Finally, the combination of these features results in the deterioration of the pinning properties of the ceramic samples at the intragranular level. Once the SPT samples were subjected to the PAHT, the superconducting properties are partially restored and the increase in the post-annealing time seems to maintain unaltered values of U_0, as seen in samples ST5 and ST30.

Finally, we want to remark that the application of SPS and SPT techniques result in highly dense ceramic samples but oxygen-deficient materials, a feature that occurs not only at the intergranular level but also at the intragranular region. However, the major difference between both techniques is that in SPT the consolidated sample are not completely confined [3]. Such difference has a definite effect on the stress distribution within the samples, which consequently impact on the degree of texture of the SPT samples.

5 Conclusions

In summary, the influence of the SPT consolidation on the intragranular features of $Bi_{1.65}Pb_{0.35}Sr_2Ca_2Cu_3O_{10+\delta}$ samples has been investigated. From $H_{c2}(T)$ dependence, we have estimated values of the upper critical field along the *ab*-plane for all samples studied. The results indicated that the SPT process has influence on the intragranular superconducting properties of Bi-2223 materials mostly because this technique occurs under vacuum. Thus, the samples were subjected to an additional post-annealing heat treatment, resulting in a 3.5-fold increase of the effective intragranular pinning energy at zero temperature and applied magnetic field. Based on these findings, we primarily concluded that the SPT process is responsible for a deoxygenation within the grains of the ceramic samples, a process that occurs predominantly near at the edge of planar defects. However, further studies are needed to confirm this belief.

Acknowledgements The authors acknowledge financial support from Brazil's agencies FAPESP (Grants Nos. 2013/07296-2, 2013/20181-0, and 2014/19245-6), CNPq (Grants Nos. 168255/2014-6, 444712/2014-3, 306006/2105-4, and 303329/2016-5), and CAPES/MES (Grants Nos. 1470/2010 and 157/2012), and the Petrobras company.

References

1. O. Guillon, J. Gonzalez-Julian, B. Dargatz, T. Kessel, G. Schierning, J. Räthel, M. Herrmann, Adv. Eng. Mater. **16**, 830–849 (2014)
2. M.Z. Becker, N. Shomrat, Y. Tsur, Adv. Mater, **30**, e1706369 (2018)
3. J.G. Noudem, D. Kenfaui, D. Chateigner, M. Gomina, Scr. Mater. **66**, 258–260 (2012)
4. L. Pérez-Acosta, E. Govea-Alcaide, J.G. Noudem, I.F. Machado, S.H. Masunaga, R.F. Jardim, Ceram. Int. **42**, 13248–13255 (2016)
5. E. Govea-Alcaide, I.F. Machado, R.F. Jardim, J. Appl. Phys. **117**, 043903–043907 (2015)
6. E. Govea-Alcaide, I.F. Machado, M. Bertolete-Carneiro, P. Muné, R.F. Jardim, J. Appl. Phys. **112**, 113906–13913 (2012)
7. U. Anselmi-Tamburini, S. Gennari, J.E. Garay, Z.A. Munir, Mater. Sci. Eng. A **394**, 139–148 (2005)
8. C. Wang, L. Cheng, Z. Zhao, Comput. Mater. Sci. **49**, 351–362 (2010)
9. F. Rosales-Saiz, L. Pérez-Acosta, I.F. Machado, J.E. Pérez-Fernández, R.F. Jardim, E. Govea-Alcaide, Ceram. Int. **42**, 17482–17488 (2016)

10. I. García-Fornaris, I. Calzada, E. Govea-Alcaide, I.F. Machado, R.F. Jardim, J. Supercond. Novel Magn. **28**, 3487–3492 (2015)
11. T.T. Palstra, B. Batlogg, L.F. Scheemeyer, J.V. Waszczak, Phys. Rev. B **43**, 3756–3759 (1991)
12. I. Matsubara, H. Tanigawa, T. Ogura, H. Yamashita, M. Kinoshita, T. Kawai, Phys. Rev. B **45**, 7414–7417 (1992)
13. M.T. Escote, V.A. Meza, R.F. Jardim, L. Ben-Dor, M.S. Torikachvili, A.H. Lacerda, Phys. Rev. B **66**, 144503–144508 (2002)
14. T.T.M. Palstra, B. Batlogg, R.B. van Dover, L.F. Schneemeyer, J.V. Waszczak, Phys. Rev. B **41**, 6621–6632 (1990)
15. E.S. Vlakhova, K.A. Nenkovb, M. Ciszekc, A. Zaleskic, Y.B. Dimitrievd, Physica C **225**, 149–157 (1994)
16. M. Dogruer, Y. Zalaoglu, A. Varilci, C. Terzioglu, G. Yildirim, O. Ozturk, J. Supercond. Novel Magn. **25**, 961–968 (2012)
17. G. Yildirim, M. Akdogan, S.P. Altintas, M. Erdem, C. Terzioglu, A. Varilci, Physica B **406**, 1853–1857 (2011)
18. G. Blatter, M.V. Feigelman, V.B. Geshkenbein, A.I. Larkin, V.M. Vinokur, Rev. Mod. Phys. **66**, 1125–1388 (1994)
19. M. Hernández-Wolpez, A. Cruz-García, O. Vázquez-Robaina, R.F. Jardim, P. Muné, Physica C **525–526**, 84–88 (2016)